

# A Generalized Seismic Attenuation Compensation Operator Optimized By 2D Mathematical Morphology Filtering

Huijian Li, Stewart Greenhalgh, Bo Liu, Xu Liu, Qi Hao and Yangkang Chen

**Abstract**—Improving resolution and signal-to-noise ratio (SNR) are common goals in seismic data processing, but the two are generally in mutual opposition. A more realistic key objective is to attain robustness. In this work, we propose a novel generalized attenuation compensation operator (GACO) for enhancing seismic resolution. The new operator is controlled by two parameters. It offers improved flexibility and adaptability compared with traditional operators, which can be considered as special cases. The two-dimensional mathematical morphology filtering (2D MMF) optimized GACO is developed for attenuation compensation of low SNR seismic data with good noise immunity and robustness. A SNR coefficient based on the time-frequency domain 2D MMF is proposed for detecting the high SNR regions of seismic records for attenuation compensation and noise suppression. Therefore, the compensated seismic data has higher resolution and higher SNR after applying the new approach. Experimental results show that the proposed scheme is practical, adaptive, and effective. More importantly, it offers good noise immunity and especially robustness in processing of strongly attenuated low SNR data.

**Index Terms**—Attenuation compensation, two-dimensional mathematical morphology filtering, High resolution

## I. INTRODUCTION

Seismic signals recorded on surface or borehole monitoring instruments (e.g., seismograph stations, geophones) are affected by energy dissipation and material dispersion due to anelasticity and heterogeneity (scattering) of the medium [1]–[3]. When using such data for underground imaging, there will be reduced accuracy and resolution, compounded with uncertainty and possible interpretation illusions. Thus, it is necessary to apply attenuation compensation for higher imaging fidelity [4]–[6]. The seismic inverse  $Q$  filtering approach which is commonly used in attenuation compensation applies a wave propagation inversion procedure that compensates for energy absorption and corrects wavelet distortion caused by velocity dispersion. By compensating for amplitude attenuation with a viscoelastic attenuation model, seismic data can provide true amplitude information for amplitude inversion and subsequent reservoir characterization. In addition, by correcting the phase distortion caused by velocity dispersion,

H. Li is with the College of Petroleum Engineering and Geosciences, King Fahd University of Petroleum and Minerals, Dhahran, Saudi Arabia; Stewart Greenhalgh is with the Institute of Geophysics, ETH Zurich, Zurich, Switzerland; B. Liu is with the Electrical Engineering Department, King Fahd University of Petroleum and Minerals, Dhahran, Saudi Arabia; X. Liu is with the College of Petroleum Engineering and Geosciences, King Fahd University of Petroleum and Minerals, Dhahran, Saudi Arabia; Y. Chen is with the Bureau of Economic Geology, The University of Texas at Austin, Austin, Texas, USA.; Qi Hao is with the College of Petroleum Engineering and Geosciences, King Fahd University of Petroleum and Minerals, Dhahran, Saudi Arabia.

the resulting seismic data with enhanced vertical resolution can provide the correct traveltime information for lithology identification.

Inverse  $Q$  filtering is derived from downward continuation of the wavefield. For each successive downward step, the extrapolated wavefield is solved as an inverse problem, which incorporates stability into the solution. This technique includes two components, the amplitude compensation and the phase correction. Whereas the phase compensation is unconditionally stable, the amplitude compensation operator is an exponential function of frequency and propagation time. Including it in the inverse  $Q$  filter may cause instability and generate undesirable artifacts. Therefore, in any inverse  $Q$  filtering scheme, stability is the main issue. Wang proposed a stabilized inverse  $Q$  filtering algorithm by using the stabilization factor  $\sigma^2$  [7]–[9].

Another attenuation compensation method is the recently developed  $Q$ -compensated reverse-time migration ( $Q$ -RTM) procedure [10]–[12]. This method is more flexible for structural imaging in the presence of steep dips and strong velocity contrasts [13]. It is based on the full seismic wavefield computation compared with the simple raypath-based (or 1D wave equation) inverse  $Q$  filtering. Both compensation methods suffer from the same difficulty, that is, the stability of the attenuation-compensated result. Since the analytical compensation function is exponential, the high-frequency components tend to be unstable. For stable compensation, application of a low-pass filter or other kinds of stabilized compensation operators have been used for inverse  $Q$  filtering [14]–[17]. By comparison,  $Q$ -RTM focuses more on the accuracy of steep dip imaging, while paying less attention to the stability of compensation by using a low-pass filter [10], [11], [18]. Recently, some stable and improved  $Q$ -RTM methods have been developed, following the concept of robust compensation operators in inverse  $Q$  filtering [19]–[22]. The imaging principle of  $Q$ -RTM is relatively mature, but its main drawback has been trading off the stability of strong attenuation compensation with noise immunity. Hence, whether implementing inverse  $Q$  filtering or  $Q$ -RTM, the key factor is the compensation operator, which determines the final imaging resolution and reliability.

The near surface zone of the Earth is usually highly variable and complex. The loose, unconsolidated formations often result in strong attenuation of seismic waves and noisy data sets. Moreover, the level of energy attenuation in the near-surface layers is often equal to or greater than the degree of attenuation in the middle and deep layers despite the much

shorter propagation distances involved in the near-surface zone [23], [24]. This emphasizes the importance of near-surface attenuation compensation. The associated problems are also more challenging. Compensation for strong attenuation is prone to instability of the resulting high-frequency components, and the influence of random and source-generated noise aggravates the robustness of the compensation result. When the signal-to-noise ratio (SNR) of certain frequency components is low, it is the noise that is essentially amplified instead of signal energy compensation. Therefore, during attenuation compensation, adaptive frequency band compensation and appropriate SNR constraints are necessary.

Enhancing *the* SNR has been achieved through various novel algorithms such as those based on mathematical transformations [25]–[29], optimization algorithms [30]–[32], and artificial intelligence [28], [33]–[37]. Mathematical morphology (MM) is a new technique being applied to seismic data denoising [27], [38], [39] which entails a different approach compared to conventional signal processing techniques. Topological and geometrical continuous-space concepts are introduced by MM on both continuous and discrete data spaces. Hence, some applications of MM in seismic data processing are surprising [40]–[42]. In view of the unique edge detection effect of the MM method, we will endeavor to apply a *two-dimensional two-dimensional* (2D) MM method in the time-frequency domain to extract the regions of high SNR, to set the threshold levels and compensate more accurately.

In this work, we first revisit the commonly used inverse  $Q$  filtering method and identify the reasons for its instability in situations of strong attenuation and its effect on noise. Then we design *a generalized a generalized* attenuation compensation operator (GACO) with two parameters for controlling strong attenuation compensation. A 2D MM technique in the time-frequency domain is also introduced for SNR calculation and attenuation compensation area optimization. The adjustable attenuation compensation operator can make reasonable compensation according to different SNR segments of the data by the 2D MM technique. This combination of two processes is intended to ensure stable signal compensation whilst improving the SNR. Finally, we use synthetic and field datasets to illustrate the efficacy, feasibility, and stability of the proposed method and to evaluate its performance.

This paper is organized as follows. The GACO scheme is presented in Section II. Section III presents the 2D MM optimization scheme. The synthetic and field data experiments and the results are shown in Sections IV and V. Finally, in Sections VI and VII, we present a discussion of the *limitation limitations*, validity and possible extensions of the methodology, and draw conclusions.

## II. GENERALIZED ATTENUATION COMPENSATION OPERATOR

### A. Inverse $Q$ filtering review

Inverse  $Q$  filtering can be best introduced and explained through the 1-D one-way wave equation in the frequency domain [7]:

$$\frac{\partial U(r, \omega)}{\partial r} - ik(\omega)U(r, \omega) = 0, \quad (1)$$

where  $U(r, \omega)$  is the wavefield with angular frequency  $\omega$  after a travel distance  $r$  and  $k$  is the complex wavenumber, whose imaginary part equals the attenuation coefficient  $K$ . The analytical solution of (1) with a constant  $Q$  model ( $Q > 10$ ) is [15]:

$$U(r + \Delta r, \omega) = U(r, \omega) e^{\left(\frac{\omega}{\omega_h}\right)^{-\gamma} \frac{\omega \Delta r}{v_r} \left(\frac{1}{2Qr} + i\right)}. \quad (2)$$

Here  $\gamma = (\pi Q_r)^{-1}$ ,  $Q_r$  is the intrinsic quality factor which may be viewed as depth (or traveltime) dependent and is related to the attenuation coefficient  $K$ ,  $v_r$  is the phase velocity,  $\omega_h$  is the highest possible angular frequency of the seismic record, and  $\Delta r$  is the travel distance increment.  $\Delta r$  is the product of traveltime increment  $\Delta t$  and velocity  $v_r$ :  $\Delta r = \Delta t v_r$ . (2) can then be expressed as

$$U(t + \Delta t, \omega) = U(t, \omega) e^{\left(\frac{\omega}{\omega_h}\right)^{-\gamma} \frac{\omega \Delta t}{2Qr} e^{i\left(\frac{\omega}{\omega_h}\right)^{-\gamma} \omega \Delta t}}. \quad (3)$$

The first exponential term is the amplitude attenuation (energy absorption), and the second term is the phase change (velocity dispersion). Extending by downward continuation from the surface  $t_0 = 0$  to the traveltime  $t$  using (3), the wavefield  $U(t, \omega)$  in time-frequency space becomes:

$$U(t, \omega) = U(0, \omega) e^{\int_0^t \left(\frac{\omega}{\omega_h}\right)^{-\gamma(\tau)} \frac{\omega}{2Q(\tau)} d\tau} \times e^{i \int_0^t \left(\frac{\omega}{\omega_h}\right)^{-\gamma(\tau)} \omega d\tau}, \quad (4)$$

where  $\gamma(\tau) = \frac{1}{\pi Q(\tau)}$ , and  $Q(\tau)$  is the  $Q$  value at time  $\tau$ . This is the basic inverse  $Q$  filter for downward continuation of all plane waves in the frequency domain. So, the compensation operators for amplitude and phase, viewed as an inverse filter (deconvolution) problem, are

$$\mathcal{A}(t, \omega) = \exp \left[ - \int_0^t \left(\frac{\omega}{\omega_h}\right)^{-\gamma(\tau)} \frac{\omega}{2Q(\tau)} d\tau \right] \quad (5)$$

and

$$\mathcal{P}(t, \omega) = \exp \left[ -i \int_0^t \left(\frac{\omega}{\omega_h}\right)^{-\gamma(\tau)} \omega d\tau \right], \quad (6)$$

respectively. Summing up all the plane waves yields the observed time series

$$u(t + \Delta t) = \frac{1}{\pi} \int_0^\infty U(t + \Delta t, \omega) \mathcal{A}(t, \omega) \mathcal{P}(t, \omega) d\omega, \quad (7)$$

which is considered as the imaging condition for seismic migration.

The phase term in (6) is unconditionally stable for signal correction because it involves an imaginary argument in the exponent whereas the amplitude operator  $\mathcal{A}(t, \omega)$  in (5), being an exponential function of the real traveltime  $t$  and frequency  $f$ , can cause instability and artefacts. Therefore, stability of the filter is one of the major concerns in compensation for anelastic absorption. A gain-limited operator was introduced

by Bickel and Natarajan [14], similar to a low-pass filter, to combat the stability problem:

$$\mathcal{A}_B(t, \omega) = \begin{cases} \exp \left[ -\int_0^t \frac{\omega}{2Q(\tau)} d\tau \right], & \omega \geq \omega_B, \\ \mathcal{A}_B(t, \omega_B), & \omega < \omega_B. \end{cases} \quad (8)$$

where  $\omega_B$  is the angular frequency threshold. It should be set with proper consideration of the noise level in the seismic data for practical application. The SNR greatly restricts this method, with the noise level reducing the stability of the compensation filter. Subsequently, Wang [15] proposed the following stabilized inverse  $Q$  filtering scheme:

$$u(t) = 2 \int_0^\infty U(0, \omega) \Lambda(t, \omega) \mathcal{P}(t, \omega) d\omega, \quad (9)$$

where  $\Lambda(t, \omega)$  is the amplitude compensation operator (ACO) expressed as

$$\Lambda(t, \omega) = \frac{\beta(t, \omega) + \sigma^2}{\beta(t, \omega)^2 + \sigma^2}, \quad (10)$$

and

$$\beta(t, \omega) = \exp \left[ - \int_0^t \left( \frac{\omega}{\omega_h} \right)^{-\gamma(\tau)} \frac{\omega}{2Q(\tau)} d\tau \right], \quad (11)$$

where

$$\sigma^2 = \exp(-0.23G_{lim} + 1.63). \quad (12)$$

Here,  $\sigma^2$  is the stabilization factor and  $G_{lim}$  is the specified gain limit in an explicit gain-controlling scheme, which generally lies between 0 and 70 dB [8], [9]. This later-developed stable inverse  $Q$  filtering method is much more robust than the initial gain-limited compensation method for noise-free and high SNR seismic data. The noisy synthetic data with different  $Q$  values (Fig. 1(a)) are used for testing these two approaches. The stabilized inverse  $Q$  filtering scheme shows many advantages (Fig. 1(c)) compared with the gain-limited method (Fig. 1(b)). However, both methods are significantly affected by noise, resulting in compensation instability. Therefore, the noise immunity of the compensation method also determines its applicability and feasibility.

### B. Generalized Attenuation Compensation Operator

Since the subsurface medium is inhomogeneous, the degree of anelastic absorption (attenuation) will vary with the wavefront (spatial) position. Experiments have proven that the near-surface attenuation is significantly higher than that of the deeper layers. Therefore, compensation for near-surface attenuation is critically more important. Due to the near-surface noise level and attenuation characteristics, the SNR of signals passing through the near surface will be significantly decreased. Hence, it is not easy to balance the stability (maintain the relative SNR) and the compensation intensity (improve the resolution) when performing amplitude compensation. In this section, we introduce a new dual-parameter inverse  $Q$  filtering method instead of the one parameter ( $G_{lim}$ ) controlled approach. The new scheme offers better noise immunity and feasibility. As a generalization, the ACO of (10) can be

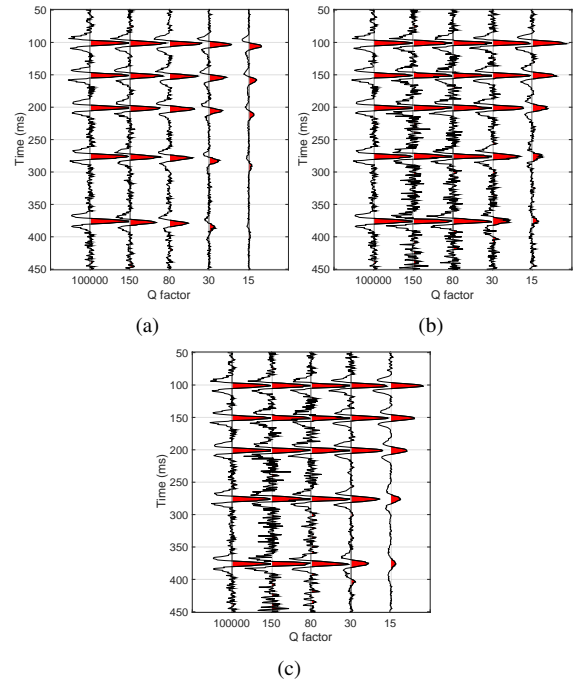


Fig. 1. Waveforms after attenuation with SNR=15 for each trace (a), gain limited compensation (b) and stabilized compensation (c) for noisy data. The main frequency of the wavelet is 50 Hz,  $Q$  value is 100000, 150, 80, 30 and 15 for weak to strong attenuation.  $G_{lim}=10$  dB.

modified and extended by the following equation with two control parameters  $m$  and  $n$ :

$$\mathcal{G}(t, \omega) = \left( \frac{\beta(t, \omega)^n + \sigma^2}{\beta(t, \omega)^m + \sigma^2} \right)^{\frac{1}{m-n}}. \quad (13)$$

For simplification, we assume the quality factor  $Q$  is time-dependent and we can make the approximation

$$\left( \frac{\omega}{\omega_h} \right)^{-\gamma(\tau)} \frac{\omega}{2Q(t)} \approx \frac{\omega}{2Q(t)}, \quad (14)$$

when  $Q(t) \gg 1$ . Then  $\beta(t, \omega) = e^{-\alpha\omega}$ , where  $\alpha = \frac{t}{2Q(t)}$  for  $Q > 10$ . For near-surface seismic data, it may be unreasonable to assume that the  $Q$  factor is greater than 10 (because attenuation is often severe in the overburden), so the above equations could induce errors. Without making the approximation or high value assumption on  $Q$ , the attenuation coefficient  $K$  is exactly related to  $Q$  through the following equation [43]:

$$\frac{1}{Q} = \frac{Kv}{\frac{\omega}{2} - \frac{K^2 v^2}{2\omega}}. \quad (15)$$

Here  $v$  is the wave velocity. According to the physical meaning of  $Q$ ,  $v$ ,  $f$  and  $K$ , whose values are all positive, we obtain:

$$K = \frac{\omega(\sqrt{Q^2 + 1} - Q)}{v}. \quad (16)$$

Then,

$$\beta(t, \omega) = e^{-Kx} = e^{-\omega(\sqrt{Q^2 + 1} - Q)}. \quad (17)$$

From a mathematical point of view, with no restriction or assumption on  $m$  and  $n$ , the derivation of (13) with respect to  $\omega$  is

$$\begin{aligned}\mathcal{G}(t, \omega)' &= \left( \frac{\beta(t, \omega)^n + \sigma^2}{\beta(t, \omega)^m + \sigma^2} \right)^{\frac{1}{m-n}}' \\ &= \frac{-n\alpha\beta^n(\beta^m + \sigma^2) + m\alpha\beta^m(\beta^n + \sigma^2)}{(m-n)(\beta^m + \sigma^2)^2}.\end{aligned}\quad (18)$$

Setting (18) equal to zero, we obtain

$$n\beta^n(\beta^m + \sigma^2) - m\beta^m(\beta^n + \sigma^2) = 0. \quad (19)$$

Suppose one of the solutions is the peak angular frequency  $\omega_s$ , then

$$\beta_s = e^{-\alpha\omega_s}, \sigma_s^2 = \frac{(n-m)\beta_s^{n+m}}{m\beta_s^n - n\beta_s^m}. \quad (20)$$

Substituting (20) into (13) yields:

$$\begin{aligned}\mathcal{G}(t, \omega) &= \frac{\beta_s^n + \frac{(n-m)\beta_s^{n+m}}{m\beta_s^n - n\beta_s^m}}{\beta_s^m + \frac{(n-m)\beta_s^{n+m}}{m\beta_s^n - n\beta_s^m}} \\ &= \frac{m}{n} \frac{1}{\beta_s^{m-n}}.\end{aligned}\quad (21)$$

Under normal conditions,  $m - n = 1$ , then the above equation can be simplified to

$$\mathcal{G}(t, \omega) = \frac{n}{n+1} \frac{1}{\beta_s(t, \omega)} \equiv \eta \frac{1}{\beta_s(t, \omega)}, \quad (22)$$

where we define  $\eta = \frac{n}{(n+1)}$  as the amplitude compensation coefficient (ACC) and  $f_s = \frac{\omega_s}{2\pi}$  is the peak frequency (PF). Hence, the GACO can be deduced from (22) with two parameters: the amplitude compensation coefficient  $\eta$  and the peak frequency  $f_s$ . Fig. 2 shows how the GACO varies with the peak frequency (Fig. 2(a)) and ACC (Fig. 2(b)). When  $n = 1$ ,  $\eta = 0.5$ , the GACO will be simplified to ACO (10), which is a special case. With the same ACC, the GACO can change the compensation curve by adjusting the PF  $f_s$ , while the ACO is fixed (Fig. 2(a) dark dashed line). When the PF is set, the GACO can also adjust the ACC to suppress the low SNR band, while giving sufficient compensation to the high SNR components (Fig. 2(b) black dashed line).

For the conventional stabilized compensation operator,  $n = 1$  and  $m = 2$ , means that the compensation amplitude is half of  $\beta^{-1}$ , which is a particular case of (21) or (22). The stabilization parameter  $\sigma^2$  is difficult for users to associate with the specific morphological characteristics of the compensation curve. It has a crest factor amplitude along with its corresponding PF. Using one parameter to control two different attributes at the same time is invariably imperfect. In this general method, the two-parameter compensation operator is designed to obtain compensation curves with varying peak amplitudes and PFs. Simultaneously, to make the method predict the absorption compensation effect of the seismic spectrum in time, the relationship between the control parameters and the compensation curve characteristics (peak coefficient and PF) is established.

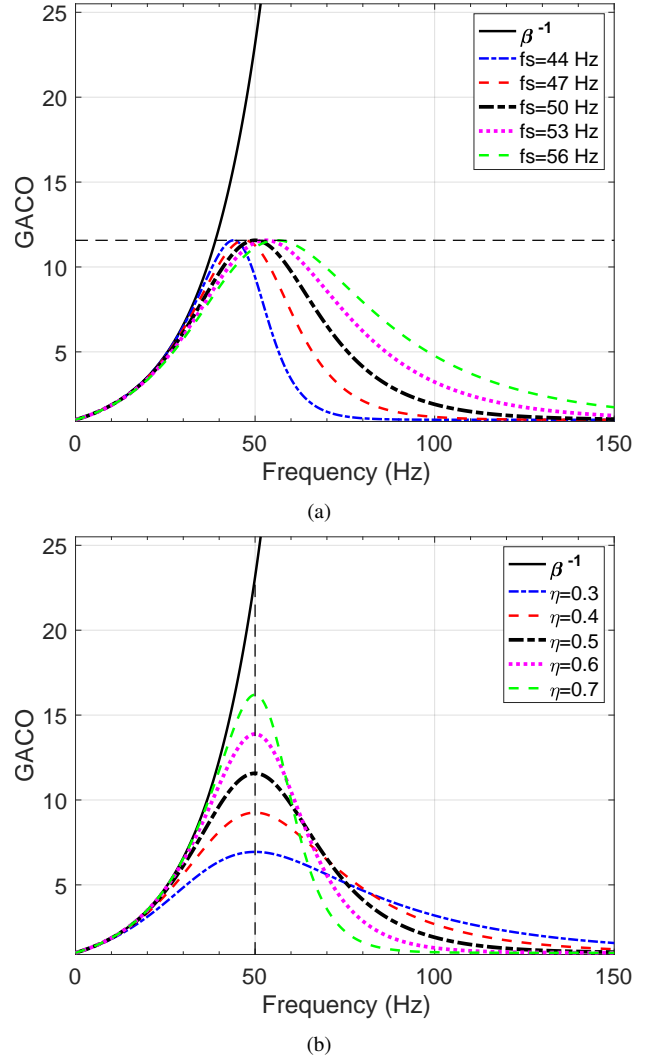


Fig. 2. GACO comparisons versus peak frequency (a) and ACC (b) with  $Q = 50$  after 1 s traveltime.

### III. TWO-DIMENSIONAL MATHEMATICAL MORPHOLOGY-BASED PARAMETER OPTIMIZATION

Estimating the high SNR segments in the time-frequency domain can help obtain more robust absorption compensation results. Owing to its special properties, MM has been developed and applied to low-frequency noise suppression [38], random noise suppression [44], [45], and coherent noise suppression [39], [46]. Therefore, in this paper we seek to apply MM to accurately extract stable SNR or high SNR segments of the data as the areas for attenuation compensation, combined with the proposed GACO, to optimize the results.

The one-dimensional MM technique has already been introduced by Li [38] for low-frequency noise suppression. The two operations of dilation and erosion form the basic elements of this method. A series of seismic data  $f(t)$  ( $t \geq 0$ ) dilated by a structural element (SE)  $s(x)$  in the time domain can be expressed as [38], [46]:

$$f(t) \oplus s(x) = \max_{x \in [0, a]} \{f(t+x) + s(x)\}, \quad (23)$$

where  $a$  is the length of the SE. Similarly, the operator of erosion is defined by

$$f(t) \ominus s(x) = \min_{x \in [0, a]} \{f(t+x) - s(x)\}. \quad (24)$$

The subsequent operators of opening (closing) are defined by the sequential combination of erosion (dilation) and dilation (erosion). Openclose (closeopen) is the opening before closing (opening). One thing to be cautious about is the drift phenomenon of the calculation results. The outcomes of dilation or erosion are expected to have a smooth effect on the SE. Considering a semi-elliptical SE with a maximum value  $s(a/2)$  at the middle point of  $a$ , the expansion result of the first element for  $f(0)$  is expected to be the sum of this value and  $s(a/2)$ . In (23), the first value is the sum of  $f(0)$  and  $s(0)$ , which is smaller than the expected value and results in drift. For this reason,  $f(x)$  should be extended before  $t = 0$  and have its value less than or equal to  $f(0)$ . The erosion calculation also needs to be extended, but its value should be greater than or equal to  $f(0)$ . Therefore, extending the input function with half of the SE length and being equal to  $f(0)$  can avoid the effect of drift. Similarly, the end of the input data also needs to be extended with half of the SE. It is worth noting that the length of the SE is preferably an odd number ( $a = 2k + 1 : k \in \mathbb{Z}$ ). The modified dilation and erosion operators can be expressed as

$$f(t) \oplus s(x) = \max_{x \in [0, a]} \{f(t-h+x) + s(x)\}, \quad (25)$$

and

$$f(t) \ominus s(x) = \min_{x \in [0, a]} \{f(t-h+x) - s(x)\}. \quad (26)$$

where  $h = \frac{a+1}{2}$ , and the input signal  $f(t)$  has been expanded to

$$f(t) = \begin{cases} f(0), & t \in \left[-\frac{a+1}{2}, 0\right], \\ f(t), & t \in [0, l], \\ f(l), & t \in [l, l + \frac{a+1}{2}]. \end{cases} \quad (27)$$

where  $l$  is the length of  $f(t)$  before expansion. The drifts are observed by means of a simple Ricker wavelet data example in Fig. 3(a). The floating distance of erosion and dilation is the length of the SE from the red and blue dashed lines in Fig. 3(a), whereas the opening and closing operations (see below) do not increase the drift. The openclose and closeopen operations are the subsequent effects of twice erosion and dilation operations, which increases the drift by twice the SE length. Therefore, the number of erosion and dilation operations determines the drift distance. Fig. 3(b) shows the results of the operators using drift correction (25) and 26. The error has been eliminated, showing the correct calculation results, and explaining the effect of different morphological operators.

Based on the above-mentioned improved 1D morphological operators, we propose a modified 2D morphological dilation and erosion operator, defined as

$$\begin{aligned} F_{dil}(t, \omega) = \\ \max_{x,y} \{F(t-h+x, \omega-g+y) + S(x, y)\}, \end{aligned} \quad (28)$$

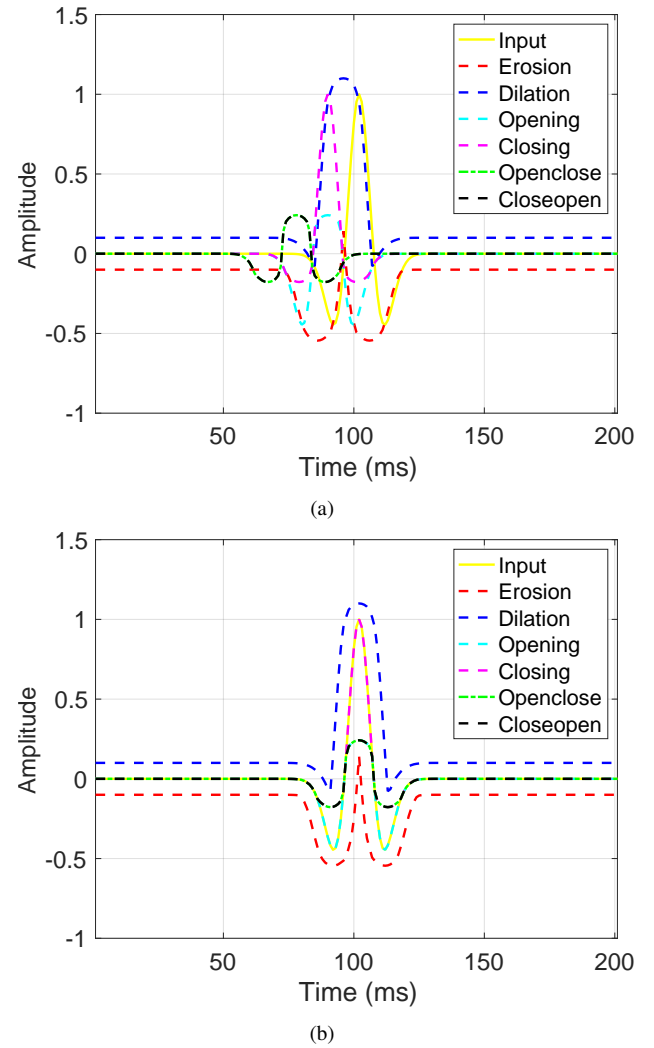


Fig. 3. The drifts of different morphological operators (a) and the corrected operators (b).

$$\begin{aligned} F_{ero}(t, \omega) = \\ \min_{x,y} \{F(t-h+x, \omega-g+y) - S(x, y)\}. \end{aligned} \quad (29)$$

where  $F(t, \omega)$  is the input seismic data in the time-frequency domain,  $\omega$  is the angular frequency,  $S(x, y)$  is the ellipsoid SE with lengths of  $a$  and  $b$ . The extended lengths are  $h = (a+1)/2$  and  $g = (b+1)/2$ . The ellipsoid SE (Fig. 4) is used for 2D MM and delineating high SNR area locations, which can be expressed as

$$\begin{aligned} SE = \\ \left| A \sqrt{\left[ 1 - \left( \frac{(x-1)}{a-1} - \frac{1}{2} \right)^2 \right] \left[ 1 - \left( \frac{(y-1)}{b-1} - \frac{1}{2} \right)^2 \right]} \right|, \end{aligned} \quad (30)$$

where  $A$  is the maximum amplitude of the SE.

The 2D mathematical morphology filtering (MMF) is de-

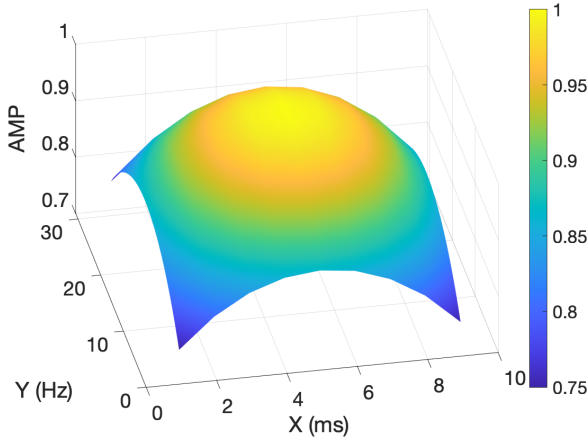


Fig. 4. The 2D ellipsoid SE time-frequency seismic spectra 2D MMF.

fined by

$$F_{MMF}(t, f) = \frac{F(t, f) \bullet SE \circ SE + F(t, f) \circ SE \bullet SE}{2}, \quad (31)$$

where  $\circ$  is 2D opening operator defined as 2D erosion before

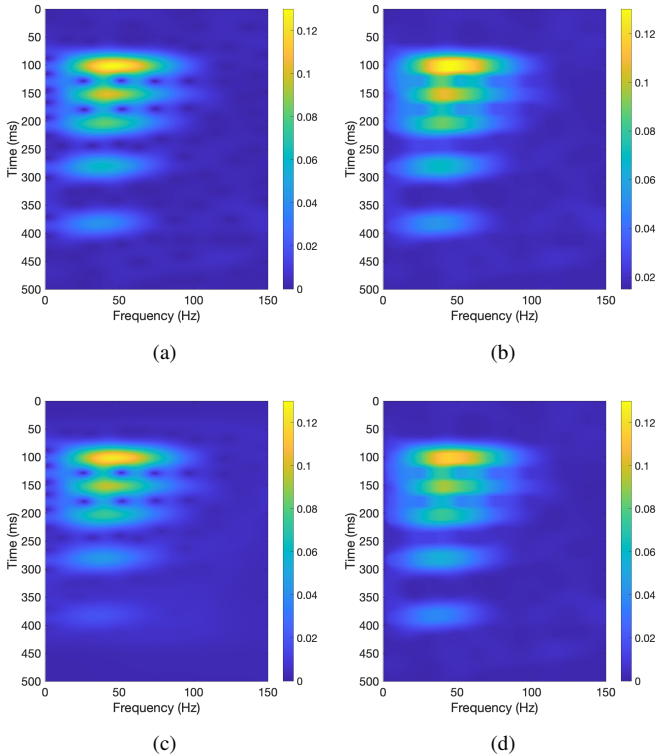


Fig. 5. The results of different 2D filters: (a). The input time-frequency spectra; (b). 2D MMF results by using ellipsoid SE with length of 25 and 5; (c). 2D wiener filtering result with parameters [91, 159]; (d). 2D median filtering by [31, 9].

2D dilation,  $\bullet$  is 2D closing operator defined as 2D erosion after 2D dilation. Fig. 5 shows the *input time-frequency spectra and the filtering* results after three different approaches: 2D MMF (Fig. 5(b)), a 2D adaptive Wiener filter (Fig. 5(c)) and

2D median filtering (Fig. 5(d)). The input data is the 4<sup>th</sup> trace in Fig. 1(a) with a SNR = 10. After such preliminary two-dimensional filtering processes, the distribution of the strong and weak areas of the SNR still cannot be properly outlined. To express the high SNR area more definitively and accurately, we propose a ratio coefficient defined by

$$H(t, f) = 100 \frac{\text{Coef}}{\text{Range}(\text{Coef})}, \quad (32)$$

where

$$\text{Coef} = \exp \left| \frac{\max(R)^2 - R^2}{\text{Range}(R)} \right|, \quad (33)$$

where  $R = 10 \log \frac{F_{MMF}(t, f)}{F(t, f)}$ , Range( $R$ ) is the range of  $R$  given by the difference between the largest and smallest values of  $R$ . Quantity  $R$  is the amplitude ratio of filtered results to the input time-frequency spectra. Fig. 6 shows the estimated ratio by three different filters. The 2D MMF (Fig. 6(a)) shows a clearer distribution and boundary for the signals compared to the 2D Wiener filter (Fig. 6(b)) and the 2D median filter (Fig. 6(c)). This indicates that the ratio coefficient obtained by 2D MMF is accurate, feasible and noise resistant. (32) and (33) enable enlargement of the feature scaling for the interesting high SNR segments of the data for attenuation compensation. The final compensation operator is determined by combining (22) and (32).

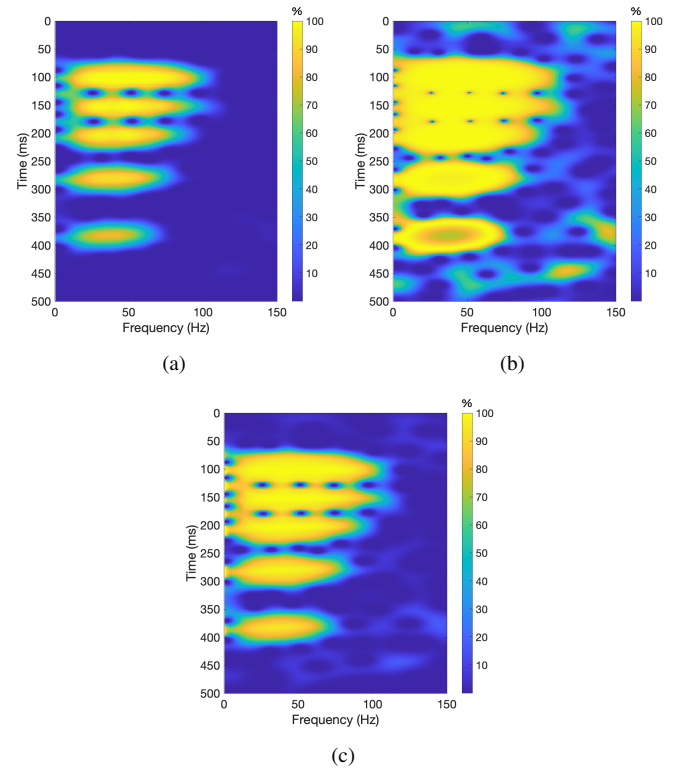


Fig. 6. Ratio coefficients  $H$  obtained by 2D MMF (a), 2D Wiener filter (b) and 2D median filter (c).

In addition, the SNR coefficient  $H$  of 2D MMF can also be directly used for noise suppression in the time-frequency domain of seismic data. That is, the smoothness and continuity

of different frequency bands are considered, and the continuity of different vertical signals is also estimated. However, comparing the plot in Fig. 5, it can be seen that the 2D MMF cannot effectively suppress noise significantly, and the result is not much different from other 2D filtering methods. Crucially however, our proposed SNR coefficient  $H$  can effectively amplify the filtering effect, which yields better results than the others. Hence, a more accurate high SNR region can be obtained (Fig. 6).

#### IV. SYNTHETIC DATA EXPERIMENTS

In this section, we validate the proposed method by synthetic data experiments. The first application uses simple one-way attenuated wave propagation records (Fig. 7(a)) with different  $Q$  factors as shown in Fig. 7(b). Random noise is added to make the  $\text{SNR} = 10$  (based on amplitude ratios, similarly hereafter) for the attenuated records. The central frequency of the Ricker wavelet is 30 Hz. It can be noticed that the attenuation is stronger with the  $Q$  factor decreasing, and the SNR of the seismic records after longer traveltimes become correspondingly lower. Therefore, it is more difficult to compensate for recordings with low SNR under strong attenuation conditions.

Fig. 7(c) shows the results using the stabilized compensation method proposed by Wang [7] with  $G_{lim} = 10$  dB. The noise has been amplified after absorption compensation compared with the first trace which is almost uncompensated (lossless) **data**. By comparison, the results of the generalized compensation method (Fig. 7(d)) are more robust, which can effectively compensate the signal whilst also ensuring that the SNR is preserved as much as possible. Inevitably, however, there will be enlarged side lobes or artifacts in some locations, especially the those areas with strong attenuation and low SNR. To address this challenge, we apply the *coefficient H based on* 2D MMF method with generalized compensation to the noisy data. The results, given in Fig. 7(e), are mostly encouraging. The strongly attenuated noisy trace ( $Q = 15$ ) is sufficiently compensated whilst preserving a relatively high SNR. The single-channel waveform comparison for trace number 5 (Fig. 8) also demonstrates the robustness and effectiveness of the proposed method, which truly achieves the simultaneous improvement of resolution and SNR. To demonstrate and highlight the superiority of the new method, the comparisons of the time-frequency spectra are provided in Fig. 9. It is obvious that the compensated spectral energy (Figs. 9(b), 9(c), 9(d)) is much stronger than the original situation (Fig. 9(a)), and the generalized approach (Fig. 9(c)) is more robust than the stabilized method (Fig. 9(b)) in maintaining a good SNR. However, to obtain fully compensated and high SNR results, the generalized compensation with 2D MMF optimization is preferred (Fig. 9(d)). Therefore, through the above comparative analysis, it is easy to conclude the superiority and robustness of the proposed method.

To demonstrate the adaptability and robustness of the generalized compensation method, a more complex synthetic data set based on the Marmousi model [47] is used. The input forward modeled data is based on the analytical solution of the

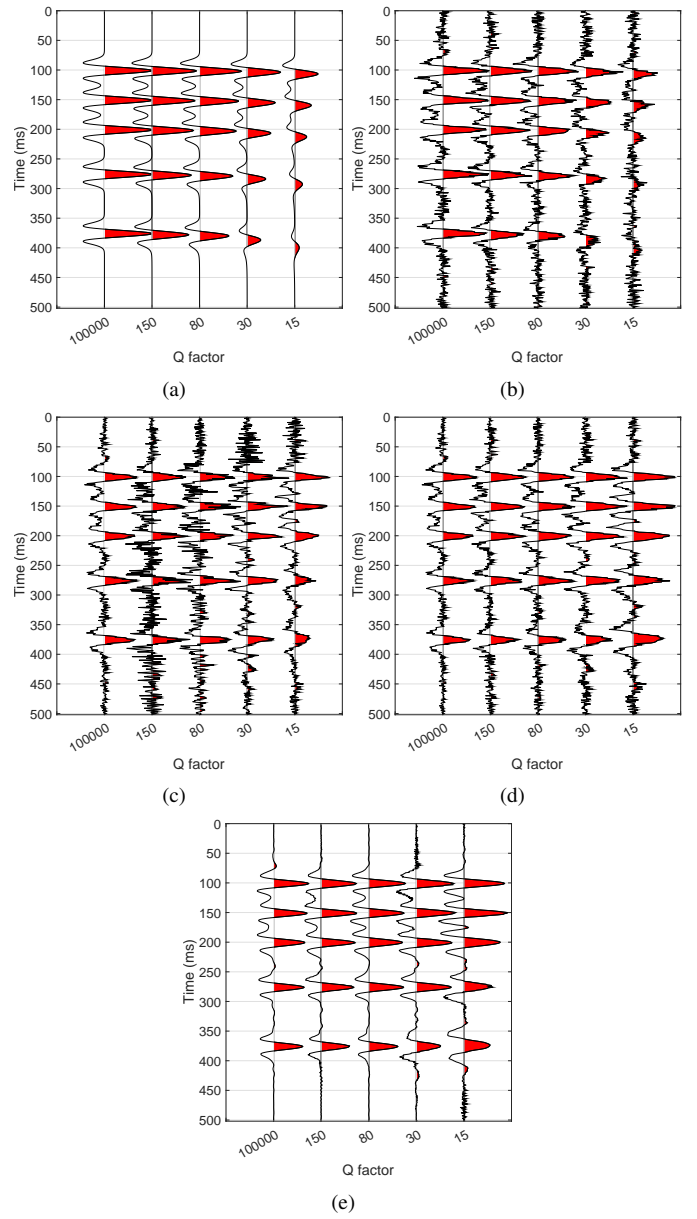


Fig. 7. The noisy records after different levels of attenuation  $\frac{1}{Q}$  (a), stabilized compensation ( $G_{lim} = 10$ ) (b), generalized compensation (c) and 2D-MMF generalized compensation (d). The noise free (a) and noisy (b) records after different levels of attenuation  $\frac{1}{Q}$ , and the results by stabilized compensation ( $G_{lim} = 10$ ) (c), generalized compensation (d) and 2D MMF generalized compensation (e).

1D one-way wave equation (4) using a Ricker wavelet source signal with the dominant frequency of 50 Hz. Fig. 10 shows the velocity and  $Q$  values of the complex geological model. The near-surface zone between the ground surface and a depth of 1300 m is characterized by low velocities (1500 ~ 2000 m/s, blue) and strong attenuation ( $Q = 16 \sim 35$ , red). There is an abnormal high-speed (5500 m/s) zone at a depth of around 2500 m on both sides of the edge, which is a low attenuation rock mass.

The modelling result is shown in Fig. 11(a). Since the near-surface velocity changes are small and the attenuation is strong, the signal amplitude is low, whereas for the mid to

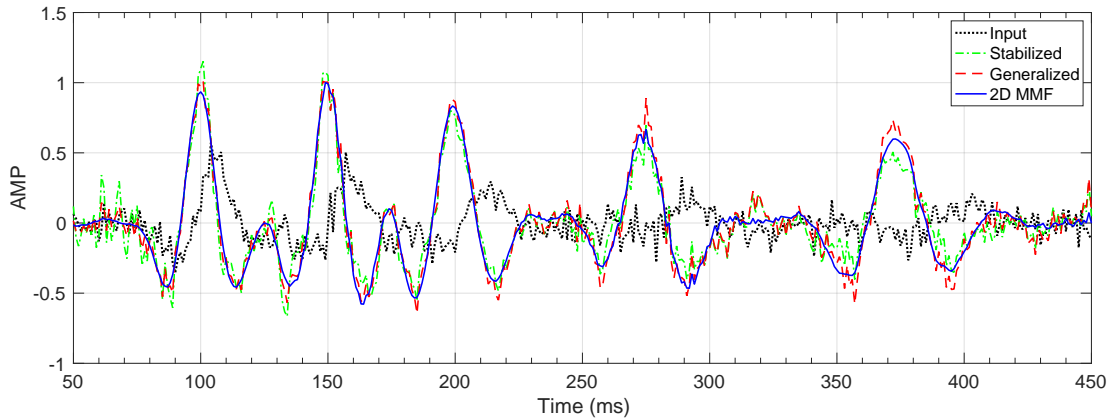


Fig. 8. Single trace comparisons after compensation by stabilized (green), generalized (red) and optimized by 2D MMF (blue) inverse  $Q$  filtering.

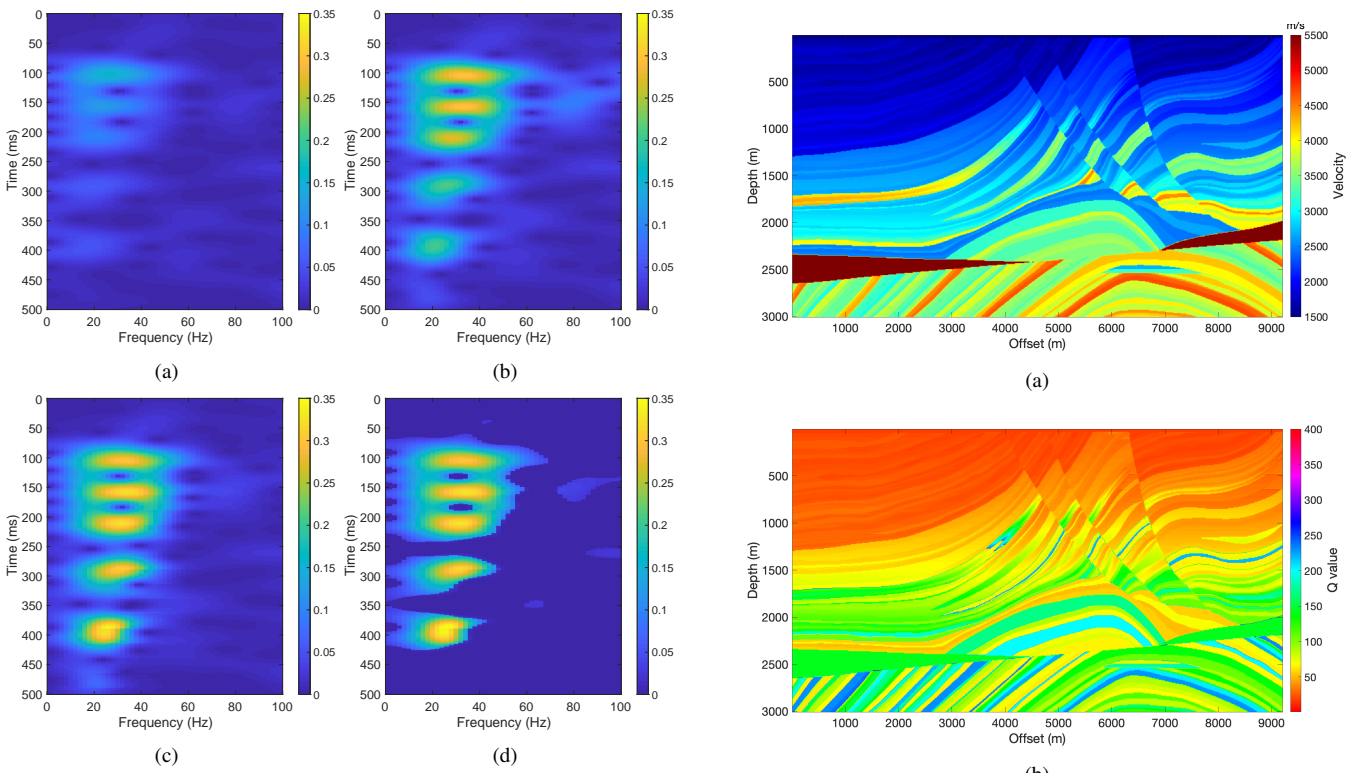


Fig. 9. Time-frequency spectra of noisy trace No. 5 (a), stabilized compensated trace No.5 (b), generalized compensated No.5 trace (c) and 2D MMF generalized compensated No.5 trace (d).

large depths the signal is the opposite with large amplitudes. Random noise has been added ( $\text{SNR} = 30$ ) to validate the robustness of different methods at high SNR. It is obvious that the proposed method using GACO is more stable and provides higher resolution compared with the stabilized inverse  $Q$  filtering method using ACO.

The zoomed compensation results reinforce and verify the previous conclusion. Fig. 12(a) shows the modeling results from the acoustic wave equation without attenuation, which is used as a reference standard for comparisons. Comparing the results of ACO (Fig. 12(b)) and GACO (Fig. 12(c)), it is easy to [find see](#) that the new approach improves the resolution with sufficient compensation, whilst suppressing or avoiding

the artifacts, as shown in the black ellipses in Fig. 12(b) and 12(c).

The single trace comparisons (Fig. 13) illustrate the superiority of the generalized compensation. Overall, the GACO results closely match the acoustic records. Locally, the results are more robust than simply using ACO, where the compensation in the high loss shallow layers is unstable due to the presence of noise.

In addition, the amplitude of noise is increased after compensation. A  $\text{SNR}=15$  data is used to simulate the compensation condition at low [noise SNR](#) levels, as shown in Fig. 14(a). The compensation time range is only from 0 to 600 ms, which is used to highlight the importance of strong near-surface

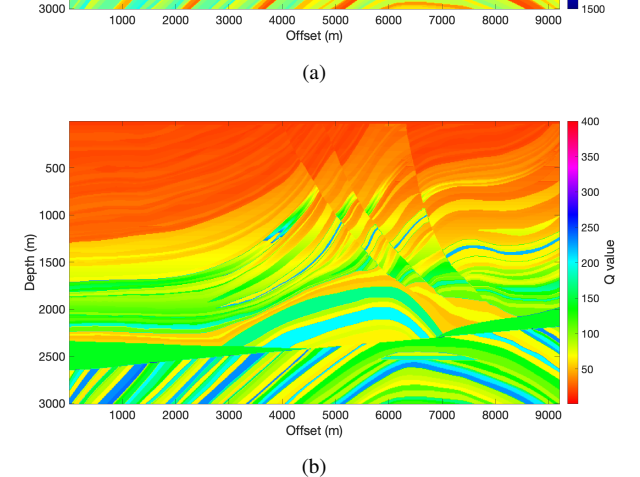
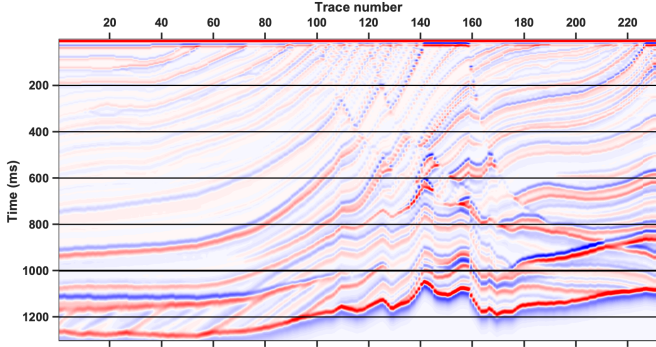
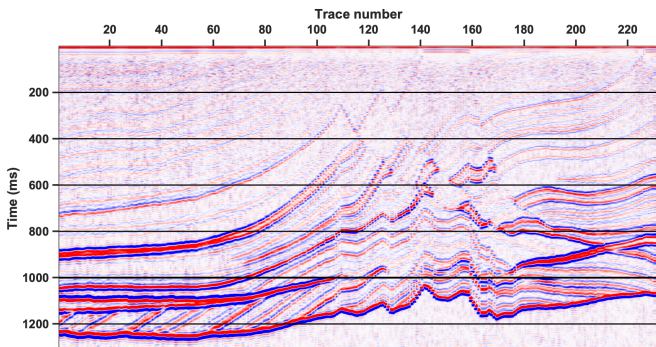


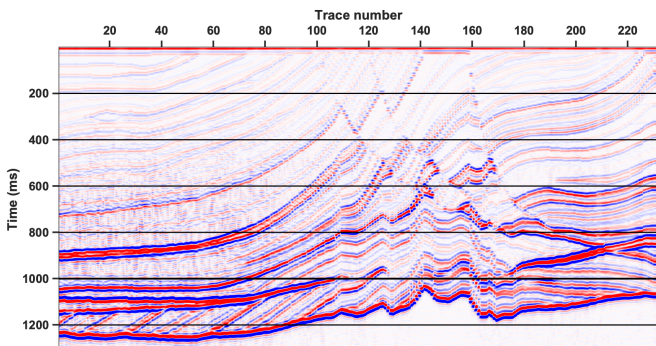
Fig. 10. The Velocity velocity (a) and  $Q$  value function values (b) for Marmousi model.



(a)



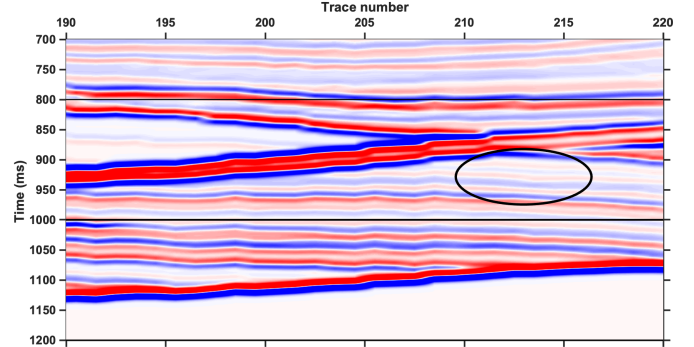
(b)



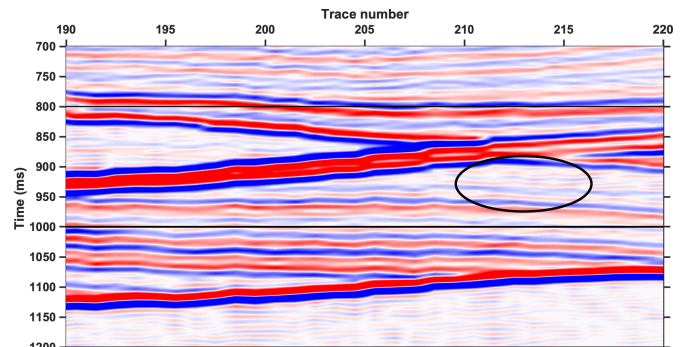
(c)

Fig. 11. The synthetic data with the Marmousi model (a), the stabilized ACO compensated result with the parameter  $G_{lim} = 42$  when SNR = 30 (b) and the GACO compensated result when SNR = 30 (c).

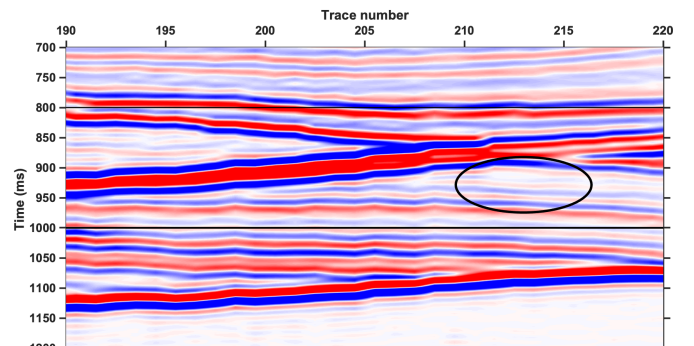
attenuation. To this end, the corresponding compensation with ACO is also reduced by  $G_{lim} = 25$ . At this point, the result of stabilized inverse  $Q$  filtering (Fig. 14(b)) yields higher resolution, but at the expense of noise amplification. The GACO result (Fig. 14(c)) is better than the ACO result, but is noisy in the mid to deep layers. To combat this issue, the 2D MMF is used to optimize GACO for attenuation compensation. Its result shows higher resolution and higher SNR after compensation, as shown in Fig. 14(d). *Some artefacts can*



(a)



(b)



(c)

Fig. 12. The zoomed acoustic records without attenuation (a), ACO compensated results (b) and GACO compensated results (c).

*also be observed, which are due to the small signal amplitude and low SNR in these areas, and the local region noise is amplified during the compensation process. Fig. 15 shows the ratio coefficient  $H$  of the No.21<sup>st</sup> trace by different methods. Compared to 2D Wiener and median filtering methods, the coefficient  $H$  based on 2D MMF provides a more reasonable and credible signal area.*

The robustness at low SNR is also confirmed in single trace comparisons in Fig. 16. At times prior to 600 ms, 2D MMF optimized GACO is consistently stable and closely matching

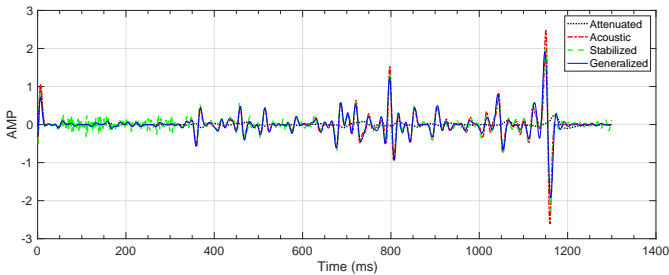


Fig. 13. Single Trace (number 115) comparisons between attenuated, acoustic, stabilized and generalized compensated waveforms with high SNR condition (SNR=30).

the unattenuated reference acoustic record (black dotted line). As the traveltimes increases beyond 600 ms, the ratio  $R$  of the compensated (inverse filtered) component to the level of attenuation (i.e. the input data) decreases, resulting in a larger discrepancy from the non-attenuated acoustic recording, but compensation of the amplitude is still clearly observed. This shows that the strong attenuation compensation near the surface is also very important, especially when the difference between its  $Q$  value and that of the deeper layers is large. As for the stabilized inverse  $Q$  filtering, it lacks robustness in the compensation of strong attenuation in the shallow layers. Therefore, GACO has good adaptability and noise immunity, whereas 2D MMF-optimized GACO offers even higher noise immunity.

## V. FIELD DATA EXPERIMENTS

In this section, our newly proposed scheme is validated on field data. We select 101 poststack seismic traces with traveltimes from 1500 to 2100 ms (Fig. 17(a)). The stable compensation results are given in Fig. 17(b) with  $G_{lim} = 20$ . Compared with the ACO compensation method, the proposed approach based on GACO (Fig. 17(c)) provides higher resolution. Specifically, detailed small faults are now clearly concentrated within the catastrophic fault zone of traces 50 ~ 100. Subsequently, the partial waveforms and time-frequency spectra of the 61<sup>st</sup> trace and its compensated results are compared in Fig. 18. For GACO compensation, the amplitude is boosted and more concentrated in the high frequencies compared to the original input data than after standard ACO compensation. Moreover, there is an obvious enhancement of the new results from 1600 ~ 2000 ms, without introducing deleterious noise, and guaranteeing a relatively high SNR.

Furthermore, we can demonstrate the robust noise immunity of our method by applying it to the noise-corrupted field data with SNR=10, as shown in Fig. 19(a). As discussed above, since the near-surface velocity changes slowly and has strong attenuation, the recorded reflection waveforms are also weak, with SNR values lower than 10. Therefore, we choose the shallow recordings from 500 ~ 1000 ms for the experiments to illustrate GACO's capability and superiority over existing approaches. Fig. 19(b) shows the records after stabilized inverse  $Q$  filtering by ACO with  $G_{lim} = 20$ . Its resolution has been improved and the noise has been suppressed, but the recordings at times above 800 ms still

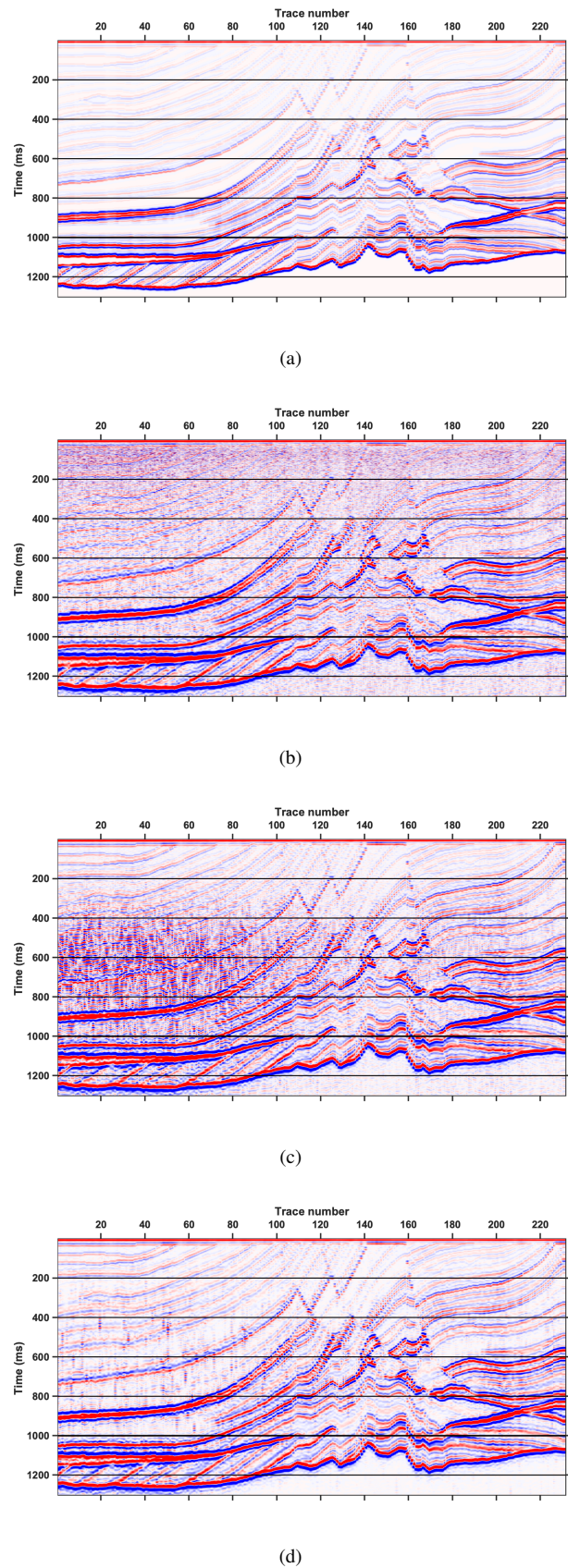


Fig. 14. The noisy synthetic data with the Marmousi model (a), the stabilized ACO compensated result with the parameter  $G_{lim} = 25$  when SNR=15 (b), the GACO compensated (c) and the 2D MMF optimized (d) results when SNR=15.

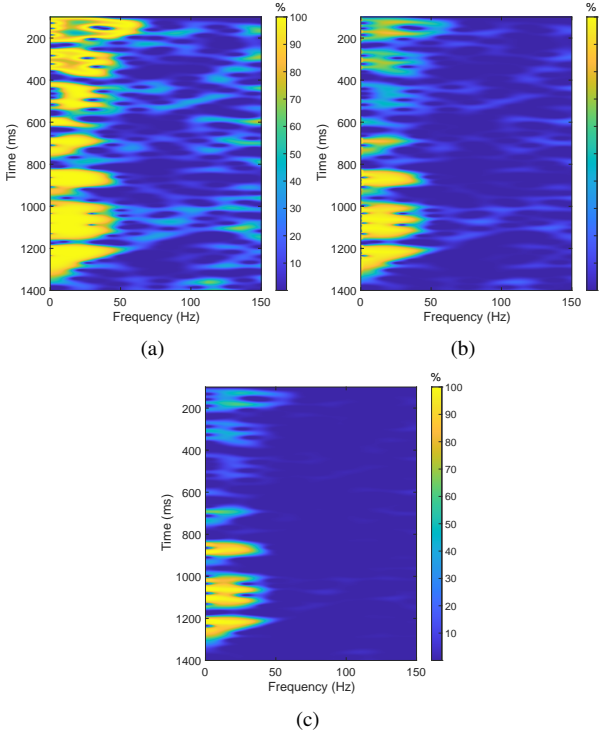


Fig. 15. Ratio coefficients  $H$  for the synthetic data with Marmousi model obtained by 2D Wiener filter (a), 2D median filter (b) and 2D MMF (c).

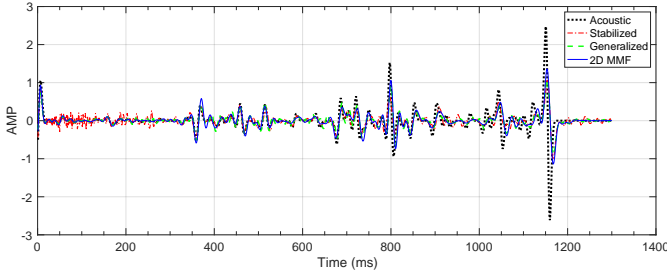


Fig. 16. Single trace (number 115) comparisons between attenuated, acoustic, stabilized and generalized compensated waveforms with low SNR condition (SNR=15).

contain a lot of noise, which is caused by the fact that the single-parameter  $G_{lim}$ -controlled ACO cannot suppress high-frequency noise very well during compensation. By contrast, as shown in Fig. 19(c), the new GACO method can effectively control the compensation of different frequencies and suppress the low SNR frequency components due to the dual-parameter control, so it provides higher resolution and a higher SNR.

Admittedly, even with this new approach applied to low SNR data, noise such as unclear, blurry, and spurious waveforms in Fig. 19(c) can be observed. To tackle such problems, the proposed GACO optimized by 2D MMF comes in handy as shown in Fig. 19(d). Compared with the first two results, the noise has been effectively controlled, and the lateral continuity has been improved. Meanwhile, the fault zone between traces 20 ~ 30 is also more clearly delineated. *Such results benefit from the ratio coefficient  $H$  based on 2D MMF (Fig. 20). It can also be seen from the figure that the high SNR segments estimated by the  $H$  coefficient based on 2D MMF (Fig. 20(c))*

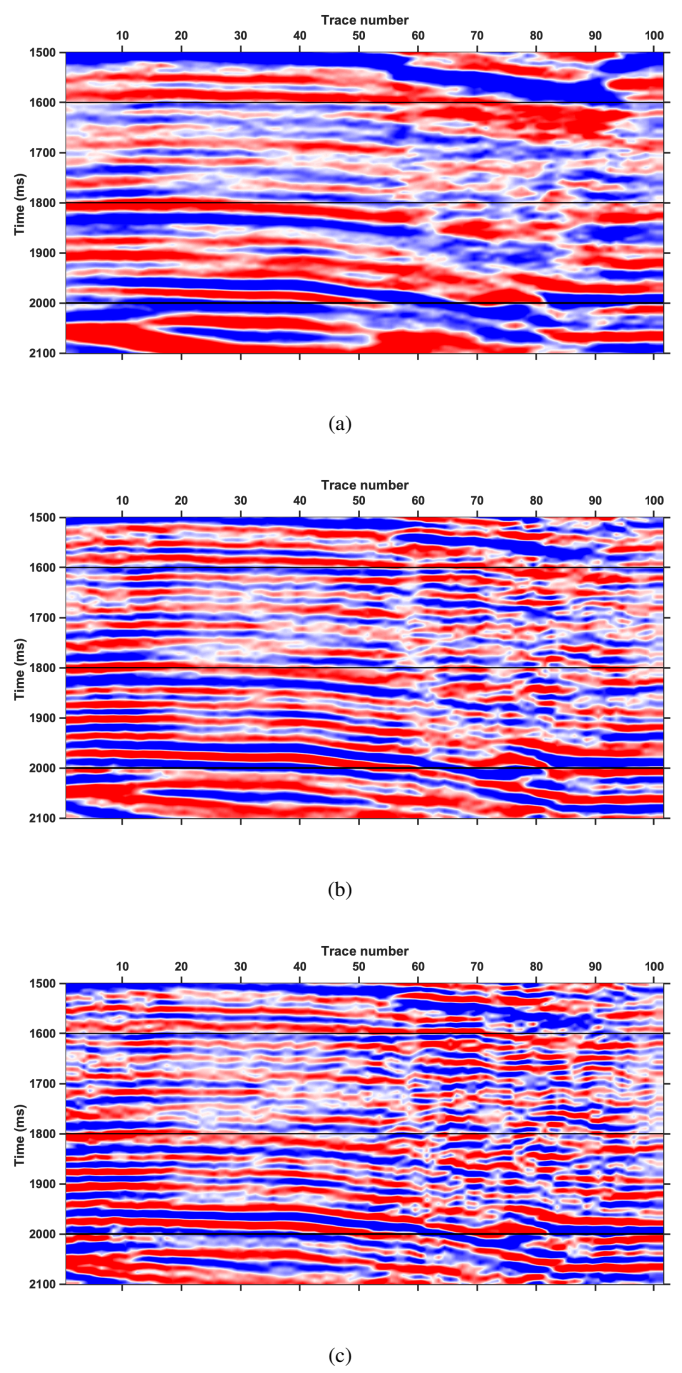
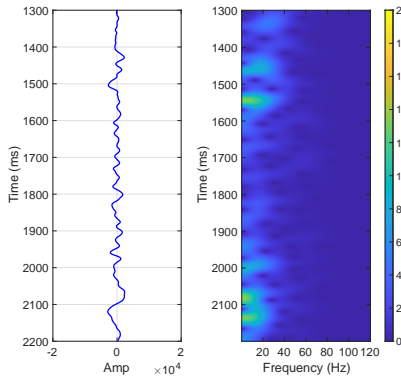


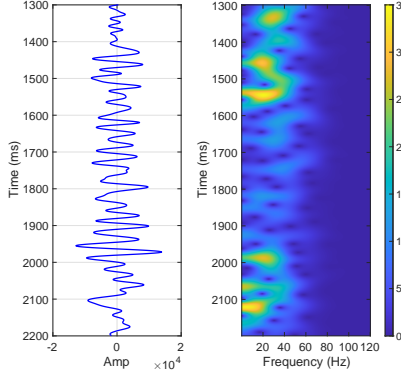
Fig. 17. (a) Section of field poststack seismic data for testing. (b) The compensation result by stabilized inverse  $Q$  filtering with  $G_{lim} = 20$ . (c) The compensation result by generalized compensation.

*are more accurate, compared to other methods (Figs. 20(a) and 20(b)).*

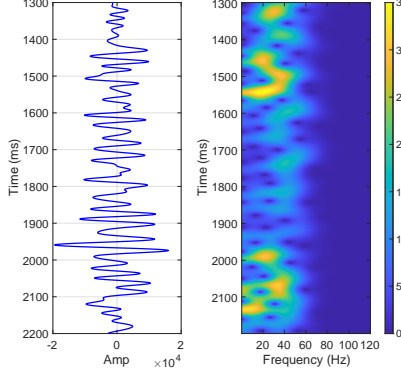
The superiority of the optimized method can also be seen from the waveform comparison in Fig. 21. The ACO method is less effective for shallow low SNR data, since it amplifies the noise and causes artifacts, but it is acceptable for relatively high SNR, weakly attenuated signals. Both the proposed GACO and 2D MMF optimization methods have good noise immunity. The latter is more capable, especially for strongly



(a)



(b)



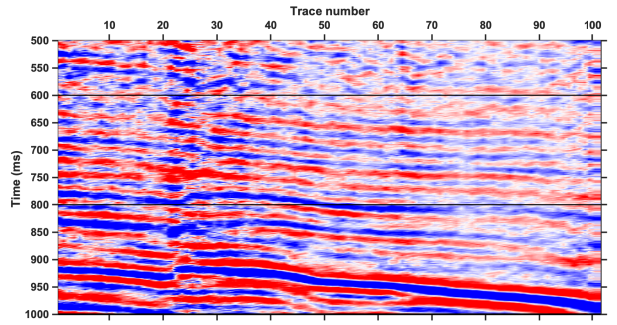
(c)

Fig. 18. Sections of the 61<sup>st</sup> trace waveform and its time-frequency spectra. (a) the input data without compensation. (b) (b) The compensated waveform by stabilized inverse  $Q$  filtering with  $G_{lim} = 20$  (c) The compensated waveform by generalized compensation.

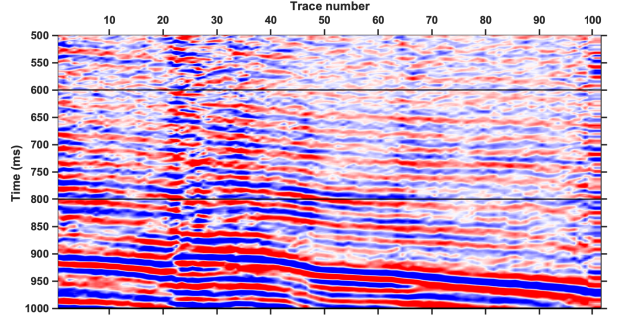
attenuated signals. It is worth noting that from this field data experiment, when the SNR is larger than 15, the GACO based approach can be directly applied to reduce the cost of 2D MMF calculation, but when the SNR is lower than 10, the 2D MMF optimized GACO method is preferable.

## VI. DISCUSSION

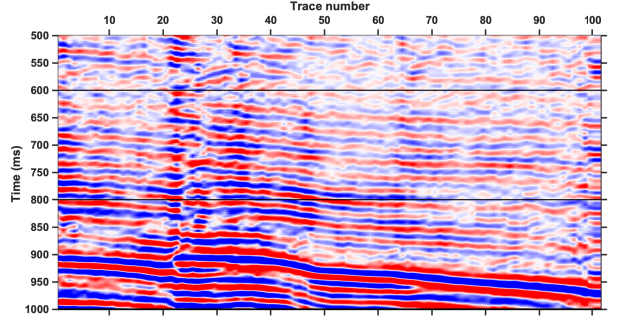
The proposed GACO is based on the extension of the stabilized operator, but theoretically has wider adaptability and controllability. Since ACO is controlled by a single parameter  $G_{lim}$  when the  $Q$  value is fixed, it is ineffective to control different SNR frequency components or cutoff frequencies. In contrast, GACO is controlled by two parameters, which



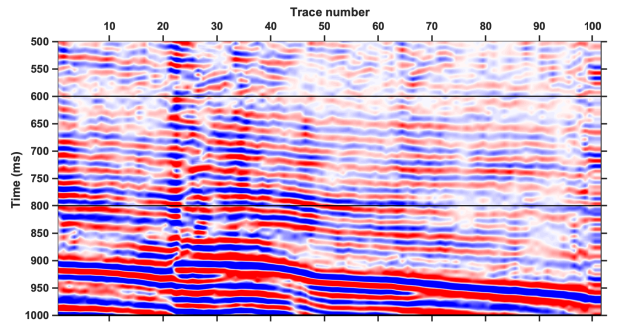
(a)



(b)



(c)



(d)

Fig. 19. (a) The noise-added field data for testing (SNR=10). (b) The stabilized ACO compensated result with the parameter  $G_{lim} = 20$ . (c) The GACO compensated result. (d) 2D MMF optimized GACO results.

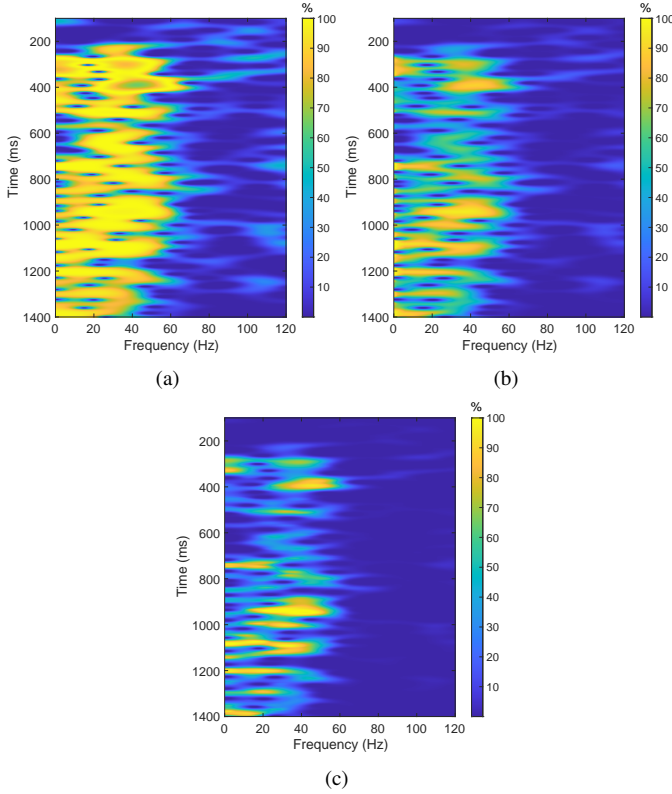


Fig. 20. Ratio coefficients  $H$  for the field data obtained by 2D Wiener filter (a), 2D median filter (b) and 2D MMF (c).

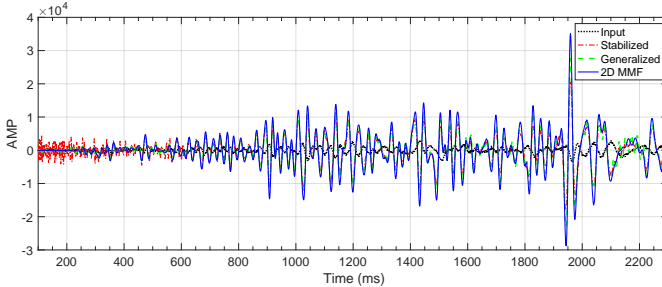


Fig. 21. Trace number 31 waveform comparisons between attenuated, stabilized, generalized compensated and 2D MMF optimized results with low SNR condition (SNR=10).

can balance amplitude compensation and cut-off frequency, to ensure an adequate compensation of signals and effective suppression of noise. Therefore, the method has higher resolution and noise immunity.

Although GACO has the advantages of being more flexible, controllable, and noise-resistant, it is still troublesome for data with low SNR. From the synthetic data examples, it can be found that although the resolution of noisy data can be improved in cases of weak noise, strong noise could still affect the results. Therefore, we developed a high-SNR area selection scheme based on 2D MMF optimization. The SNR coefficient  $H$  can effectively optimize the frequency region of high SNR while still reducing the influence of high frequency noise. The GACO provides a higher noise immunity when combined with the 2D MMF optimization. However, it is worth noting that the computational complexity of 2D MMF is much higher

than that of 1D MMF. As the size of SE becomes larger, the computational complexity will increase accordingly. For a seismic trace of size of  $2000 \times 2000$  in the time-frequency domain, the ACO compensation takes 0.96 s, the GACO takes 1.20 s, while the 2D MMF optimized GACO takes 27.2 s using an Intel i7 2.6 GHz processor with 6 cores. However, the computing time can be reduced to 6.50 s for a selected frequency band  $0 \sim 300$  Hz ( $300 \times 2000$  for the time-frequency spectrum). Therefore, for data with high SNR, the 2D MMF optimization step can be omitted to improve computational efficiency. *Recently, with the continuous development of artificial intelligence (AI) research, machine learning and deep learning techniques have also been applied to seismic data processing. The method in this paper can also be combined with these AI algorithms to improve its computational efficiency and reduce the repetitive process.*

*Similar to previous studies, the choice of morphological parameters in this research also determines the effect of the compensation method. There are three parameters of the SE: the peak amplitude  $A$ , the lengths of time and frequency windows ( $a$  and  $b$ ). As a default,  $A$  is the maximum amplitude of the selected time frequency spectra. The values of  $a$  and  $b$  are usually associated with the domain frequency  $f_0$  and the time and frequency sampling intervals ( $dt$  and  $df$ ) with  $b \in [\frac{1}{8f_0dt}, \frac{1}{10f_0dt}]$  and  $b \approx 1/f_0/df$ .*

In this paper, we mainly apply GACO to the inverse  $Q$  filtering method, but this operator can also be used in imaging methods such as  $Q$ -RTM to obtain higher horizontal and vertical resolutions. When calculating the inverse time propagation of the wavefield, the analytical solution of the amplitude-boosted compensation filter is an exponential function, that is,  $\beta^{-1}$  in this paper, which is not robust. Some methods may use ACO as a stabilization factor for amplitude-boosted wave propagation [21], obtaining more stable imaging results. Thus, GACO can also be replaced by ACO to achieve generalized robust inverse time propagation, which gives  $Q$ -RTM higher stability and noise immunity.

The pitfall of high-resolution processing is the creation and amplification of artifacts, such as the increase in virtual events. *It is* partially due to the enlarged side lobes and amplified noise. The GACO scheme is generally better for controlling noise and therefore has fewer artifacts. The compensated spectrum is an improved exponential curve, so its shape will be sharper, resulting in enlarged side lobes. The generation of this artefact is due to compensation like bandpass filtering, which can be investigated in future studies.

## VII. CONCLUSIONS

In this paper, we derived a generalized attenuation compensation operator (GACO) by extending and improving on previous research. The proposed operator is controlled by two parameters, the amplitude compensation coefficient  $\eta$  and the peak frequency  $f_s$ . Parameter  $\eta$  determines the compensation amplitude, generally in the range  $0 \sim 1$ , i.e., the amplitude at the peak frequency of the compensation is  $(\eta\beta)^{-1}$ . Parameter  $f_s$  determines the peak frequency after compensation. The traditional ACO is a special case of GACO, and its  $\eta$  is

fixed at 0.5. Therefore, GACO is theoretically more flexible and adaptable. For low SNR and strongly attenuated data, we proposed a SNR coefficient  $H$  (or  $R$ ) based on time-frequency domain 2D MMF to optimize GACO, which can effectively calculate the relatively high SNR regions of the data for energy compensation. Finally, experiments on synthetic data from a simple model, the Marmousi model, and a field data set all demonstrate the superiority of the proposed GACO and its 2D MMF-optimized algorithm over previous approaches. It offers wide adaptability and good noise immunity and is especially robust for strongly attenuated low SNR seismic data. It is worth noting that the 2D MMF optimized method requires a large amount of calculation time. Considering the high calculation cost, it should be applied only sparingly and in a timely manner according to the assessment of the SNR.

#### ACKNOWLEDGMENT

We are grateful to the College of Petroleum Engineering and Geosciences, King Fahd University of Petroleum and Minerals, Kingdom of Saudi Arabia (Grant No. SF19016) for supporting this research.

#### REFERENCES

- [1] J. Ita and L. Stixrude, "Petrology, elasticity, and composition of the mantle transition zone," *Journal of Geophysical Research: Solid Earth*, vol. 97, no. B5, pp. 6849–6866, 1992.
- [2] S. V. Sobolev, H. Zeyen, G. Stoll, F. Werling, R. Altherr, and K. Fuchs, "Upper mantle temperatures from teleseismic tomography of French Massif Central including effects of composition, mineral reactions, anharmonicity, anelasticity and partial melt," *Earth and Planetary Science Letters*, vol. 139, no. 1-2, pp. 147–163, 1996.
- [3] N. Toksoz, "Seismic wave attenuation," *Laboratory measurements*, pp. 105–114, 1981.
- [4] G. Michlmayr, D. Cohen, and D. Or, "Sources and characteristics of acoustic emissions from mechanically stressed geologic granular media—A review," *Earth-Science Reviews*, vol. 112, no. 3-4, pp. 97–114, 2012.
- [5] Y. Ricard, S. Durand, J. P. Montagner, and F. Chambat, "Is there seismic attenuation in the mantle?," *Earth and Planetary Science Letters*, vol. 388, pp. 257–264, 2014.
- [6] L. Zhao, D. Han, Q. Yao, R. Zhou, and F. Yan, "Seismic reflection dispersion due to wave-induced fluid flow in heterogeneous reservoir rocks," *Geophysics*, vol. 80, no. 3, pp. D221–D235, 2015.
- [7] Y. Wang, "A stable and efficient approach of inverse  $Q$  filtering," *Geophysics*, vol. 67, no. 2, pp. 657–663, 2002.
- [8] Y. Wang, "Inverse  $Q$ -filter for seismic resolution enhancement," *Geophysics*, vol. 71, no. 3, pp. V51–V60, 2006.
- [9] Y. Wang, *Seismic inverse  $Q$  filtering*. John Wiley & Sons, 2009.
- [10] T. Zhu, J. M. Harris, and B. Biondi, "Q-compensated reverse-time migration," *Geophysics*, vol. 79, no. 3, pp. S77–S87, 2014.
- [11] G. Dutta and G. T. Schuster, "Attenuation compensation for least-squares reverse time migration using the viscoacoustic-wave equation," *Geophysics*, vol. 79, no. 6, pp. S251–S262, 2014.
- [12] H. Wang, G. Huang, W. Chen, and Y. Chen, "Q-compensated denoising of seismic data," *IEEE Transactions on Geoscience and Remote Sensing*, vol. 59, no. 4, pp. 3580–3587, 2020.
- [13] E. Baysal, D. D. Kosloff, and J. W. Sherwood, "Reverse time migration," *Geophysics*, vol. 48, no. 11, pp. 1514–1524, 1983.
- [14] S. Bickel and R. Natarajan, "Plane-wave  $Q$  deconvolution," *Geophysics*, vol. 50, no. 9, pp. 1426–1439, 1985.
- [15] Y. Wang, "Inverse- $Q$  filtered migration," *Geophysics*, vol. 73, no. 1, pp. S1–S6, 2008.
- [16] Y. Zhao, N. Mao, and J. Xu, "Generalized stable inverse  $Q$  filtering," *Journal of Applied Geophysics*, vol. 169, pp. 214–225, 2019.
- [17] Y. Li, G. Zhang, J. Duan, C. He, H. Du, F. Luo, Y. Zhan, and J. Wang, "Extended stable factor method for the inverse  $Q$ -filter," *Geophysics*, vol. 85, no. 3, pp. T155–T163, 2020.
- [18] J. Sun, S. Fomel, T. Zhu, and J. Hu, "Q-compensated least-squares reverse time migration using low-rank one-step wave extrapolation," *Geophysics*, vol. 81, no. 4, pp. S271–S279, 2016.
- [19] Y. Wang, H. Zhou, H. Chen, and Y. Chen, "Adaptive stabilization for Q-compensated reverse time migration," *Geophysics*, vol. 83, no. 1, pp. S15–S32, 2018.
- [20] Q. Li, L.-Y. Fu, W. Wei, W. Sun, Q. Du, and Y. Feng, "Stable and high-efficiency attenuation compensation in reverse-time migration using wavefield decomposition algorithm," *IEEE Geoscience and Remote Sensing Letters*, vol. 16, no. 10, pp. 1615–1619, 2019.
- [21] H. Chen, H. Zhou, and Y. Rao, "An implicit stabilization strategy for Q-compensated reverse time migration," *Geophysics*, vol. 85, no. 3, pp. S169–S183, 2020.
- [22] J. Yang, J. Huang, H. Zhu, Z. Li, and N. Dai, "Viscoacoustic reverse time migration with a robust space-wavenumber domain attenuation compensation operator," *Geophysics*, vol. 86, no. 5, pp. S339–S353, 2021.
- [23] R. C. Aster and P. M. Shearer, "High-frequency borehole seismograms recorded in the San Jacinto Fault zone, Southern California Part 2. Attenuation and site effects," *Bulletin of the Seismological Society of America*, vol. 81, no. 4, pp. 1081–1100, 1991.
- [24] R. E. Abercrombie, "Near-surface attenuation and site effects from comparison of surface and deep borehole recordings," *Bulletin of the Seismological Society of America*, vol. 87, no. 3, pp. 731–744, 1997.
- [25] M. Naghizadeh, "Seismic data interpolation and denoising in the frequency-wavenumber domain," *Geophysics*, vol. 77, no. 2, pp. V71–V80, 2012.
- [26] J. L. Gómez and D. R. Velis, "A simple method inspired by empirical mode decomposition for denoising seismic data," *Geophysics*, vol. 81, no. 6, pp. V403–V413, 2016.
- [27] W. Huang, R.-S. Wu, and R. Wang, "Damped dreamlet representation for exploration seismic data interpolation and denoising," *IEEE Transactions on Geoscience and Remote Sensing*, vol. 56, no. 6, pp. 3159–3172, 2018.
- [28] W. Liu and Z. Duan, "Seismic signal denoising using  $f - x$  variational mode decomposition," *IEEE Geoscience and Remote Sensing Letters*, vol. 17, no. 8, pp. 1313–1317, 2019.
- [29] J. Li, N. Feng, and M. Ran, "Processing step-based adaptive seismic denoising method of transformation domain hybrid technique," *IEEE Geoscience and Remote Sensing Letters*, 2021.
- [30] S. Yuan, S. Wang, C. Luo, and T. Wang, "Inversion-based 3-D seismic denoising for exploring spatial edges and spatio-temporal signal redundancy," *IEEE Geoscience and Remote Sensing Letters*, vol. 15, no. 11, pp. 1682–1686, 2018.
- [31] O. Shao, L. Wang, X. Hu, and Z. Long, "Seismic denoising via truncated nuclear norm minimization," *Geophysics*, vol. 86, no. 2, pp. V153–V169, 2021.
- [32] F. Li, F. Sun, N. Liu, and R. Xie, "Denoising seismic signal via resampling local applicability functions," *IEEE Geoscience and Remote Sensing Letters*, 2021.
- [33] S. Beckouche and J. Ma, "Simultaneous dictionary learning and denoising for seismic data," *Geophysics*, vol. 79, no. 3, pp. A27–A31, 2014.
- [34] L. Zhu, E. Liu, and J. H. McClellan, "Seismic data denoising through multiscale and sparsity-promoting dictionary learning," *Geophysics*, vol. 80, no. 6, pp. WD45–WD57, 2015.
- [35] W. Zhu, S. M. Mousavi, and G. C. Beroza, "Seismic signal denoising and decomposition using deep neural networks," *IEEE Transactions on Geoscience and Remote Sensing*, vol. 57, no. 11, pp. 9476–9488, 2019.
- [36] O. M. Saad and Y. Chen, "Deep denoising autoencoder for seismic random noise attenuation," *Geophysics*, vol. 85, no. 4, pp. V367–V376, 2020.
- [37] L. Kuruguntla, V. C. Dodd, and K. Elumalai, "Study of parameters in dictionary learning method for seismic denoising," *IEEE Transactions on Geoscience and Remote Sensing*, 2021.
- [38] H. Li, R. Wang, S. Cao, Y. Chen, and W. Huang, "A method for low-frequency noise suppression based on mathematical morphology in microseismic monitoring," *Geophysics*, vol. 81, no. 3, pp. V159–V167, 2016.
- [39] Y. Zhou, R. Wang, and W. Huang, "Surface diffraction noise attenuation for marine seismic data processing with mathematical morphological filtering," *IEEE Transactions on Geoscience and Remote Sensing*, 2020.
- [40] W. Huang, R. Wang, H. Li, and Y. Chen, "Unveiling the signals from extremely noisy microseismic data for high-resolution hydraulic fracturing monitoring," *Scientific Reports*, vol. 7, p. 11996, 2017.
- [41] W. Huang, R. Wang, and Y. Chen, "Regularized non-stationary morphological reconstruction algorithm for weak signal detection in microseismic monitoring: Methodology," *Geophysical Journal International*, vol. 213, pp. 1189–1211, 2018.

- [42] W. Huang, R. Wang, S. Zu, and Y. Chen, "Low-frequency noise attenuation in seismic and microseismic data using mathematical morphological filtering," *Geophysical Journal International*, vol. 222, no. 3, p. 1728–1749, 2020.
- [43] E. L. Hamilton, "Compressional-wave attenuation in marine sediments," *Geophysics*, vol. 37, no. 4, pp. 620–646, 1972.
- [44] W. Huang, R. Wang, S. Wang, L. Cao, B. Yu, and G. Shang, "F–xy domain morphological filtering for three-dimensional seismic erratic noise suppression," *Geophysical Journal International*, vol. 216, no. 1, pp. 81–102, 2019.
- [45] Y. Liu and Z. Yan, "Application of a cascading filter implemented using morphological filtering and time–frequency peak filtering for seismic signal enhancement," *Geophysical Prospecting*, vol. 68, no. 6, pp. 1727–1741, 2020.
- [46] W. Huang, R. Wang, D. Zhang, Y. Zhou, W. Yang, and Y. Chen, "Mathematical morphological filtering for linear noise attenuation of seismic data," *Geophysics*, vol. 82, no. 6, pp. V369–V384, 2017.
- [47] R. Versteeg, "The Marmousi experience: Velocity model determination on a synthetic complex data set," *The Leading Edge*, vol. 13, no. 9, pp. 927–936, 1994.